2015

End-of-winter snow depth variability on glaciers in Alaska

Daniel McGrath
USGS Alaska Science Center, dmcgrath@usgs.gov

Louis Sass
USGS Alaska Science Center

Shad O/Neel
USGS Alaska Science Center

Anthony Arendt
University of Washington - Seattle Campus

Gabriel Wolken
Alaska Division of Geological and Geophysical Surveys

See next page for additional authors

AGU PUBLICATIONS

JGR

Journal of Geophysical Research: Earth Surface

RESEARCH ARTICLE

10.1002/2015JF003539

Key Points:
- SWE on Alaska's glaciers is broadly controlled by distance from moisture sources
- SWE elevation gradients are steeper than measured in nonglacierized terrain
- Thorough sampling of terrain parameters provides robust extrapolation

Correspondence to:
D. McGrath,
dmcgrath@usgs.gov

Citation:
McGrath, D., L. Sass, S. O'Neel, A. Arendt, G. Wolken, A. Gusmeroli, C. Kienholz, and C. McNeil (2015), End-of-winter snow depth variability on glaciers in Alaska, *J. Geophys. Res. Earth Surf.*, *120*, 1530–1550, doi:10.1002/2015JF003539.

Received 10 MAR 2015
Accepted 11 JUL 2015
Accepted article online 16 JUL 2015
Published online 18 AUG 2015

End-of-winter snow depth variability on glaciers in Alaska

Daniel McGrath[1,2], Louis Sass[1], Shad O'Neel[1], Anthony Arendt[3], Gabriel Wolken[4], Alessio Gusmeroli[5], Christian Kienholz[6], and Christopher McNeil[1]

[1]USGS Alaska Science Center, Anchorage, Alaska, USA, [2]CIRES, University of Colorado Boulder, Boulder, Colorado, USA, [3]Applied Physics Laboratory, University of Washington, Seattle, Washington, USA, [4]Alaska Division of Geological and Geophysical Surveys, Fairbanks, Alaska, USA, [5]International Arctic Research Center, University of Alaska Fairbanks, Fairbanks, Alaska, USA, [6]Geophysical Institute, University of Alaska Fairbanks, Fairbanks, Alaska, USA

Abstract A quantitative understanding of snow thickness and snow water equivalent (SWE) on glaciers is essential to a wide range of scientific and resource management topics. However, robust SWE estimates are observationally challenging, in part because SWE can vary abruptly over short distances in complex terrain due to interactions between topography and meteorological processes. In spring 2013, we measured snow accumulation on several glaciers around the Gulf of Alaska using both ground- and helicopter-based ground-penetrating radar surveys, complemented by extensive ground truth observations. We found that SWE can be highly variable (40% difference) over short spatial scales (tens to hundreds of meters), especially in the ablation zone where the underlying ice surfaces are typically rough. Elevation provides the dominant basin-scale influence on SWE, with gradients ranging from 115 to 400 mm/100 m. Regionally, total accumulation and the accumulation gradient are strongly controlled by a glacier's distance from the coastal moisture source. Multiple linear regressions, used to calculate distributed SWE fields, show that robust results require adequate sampling of the true distribution of multiple terrain parameters. Final SWE estimates (comparable to winter balances) show reasonable agreement with both the Parameter-elevation Relationships on Independent Slopes Model climate data set (9–36% difference) and the U.S. Geological Survey Alaska Benchmark Glaciers (6–36% difference). All the glaciers in our study exhibit substantial sensitivity to changing snow-rain fractions, regardless of their location in a coastal or continental climate. While process-based SWE projections remain elusive, the collection of ground-penetrating radar (GPR)-derived data sets provides a greatly enhanced perspective on the spatial distribution of SWE and will pave the way for future work that may eventually allow such projections.

1. Introduction

Mass loss from Alaska's glaciers (-50 ± 17 Gt/yr) is one of the largest contributions to global eustatic sea level rise outside of the Greenland and Antarctic ice sheets [*Gardner et al.*, 2013]. While regional estimates yield insight into the global mass balance distribution, the coarse-resolution remote sensing input does not enable studies of individual watersheds or the processes controlling mass balance variability. Ablation typically exhibits high spatial coherence and can be modeled using energy flux calculations and/or parameterized using automatic weather station (AWS) data [*Hock*, 2005]. In contrast, precipitation exhibits characteristically high spatial variability that is often further modified by wind redistribution. As a result, snow accumulation is difficult to either accurately measure or model on glaciers [*Pälli et al.*, 2002; *Machguth et al.*, 2006; *Sold et al.*, 2013]. Parameterizing accumulation via elevation can result in uncertainties that are estimated to be an order of magnitude larger than ablation uncertainty [*Machguth et al.*, 2006].

Thus, both our current understanding of glacier mass balance and prognostic capabilities can be improved by increased resolution of the magnitude and spatial variability of winter snow accumulation [*Huss et al.*, 2014]. Moreover, this knowledge will fill gaps in understanding across a diverse range of science and management applications beyond glacier mass balance, including water supply and quality, flood forecasting, hydropower, ocean circulation, and stratification [*Kaser et al.*, 2010; *Immerzeel et al.*, 2013; *Stabeno et al.*, 2004; *Cherry et al.*, 2010]. This is particularly true in the Gulf of Alaska (GoA) watershed, where ~50% of the estimated 800 km^3 annual freshwater runoff drains glacierized areas, of which nearly 10% is from glacier volume loss [*Neal et al.*, 2010; *Hill et al.*, 2015]. This freshwater discharge is an important source for nutrients delivered to the GoA and as such is connected to regional ecological function [*Hood and Berner*, 2009; *Hood et al.*, 2015; *O'Neel et al.*, 2014].

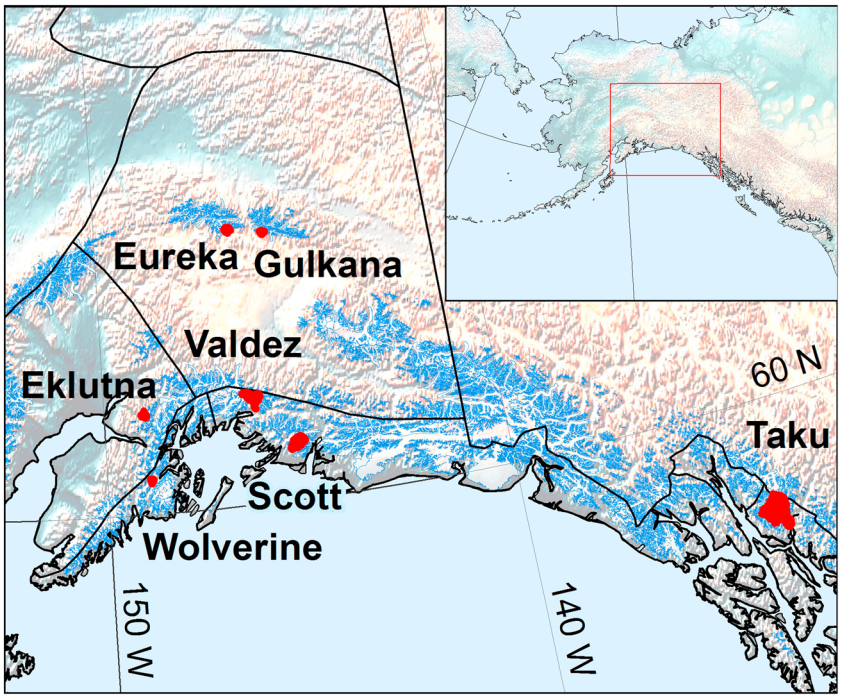

Figure 1. Location map of seven glaciers where GPR were collected during 2012–2013 winter. The glaciers are located in five different climate divisions across Alaska [*Bieniek et al.*, 2012]. Glaciers are outlined in blue [*Pfeffer et al.*, 2014] and red polygons are studies glaciers. Inset: location of study region.

The interplay between complex topography, strong orographic gradients, and wind redistribution in mountainous or glacierized environments produce complicated accumulation patterns [*Winstral et al.*, 2002; *Machguth et al.*, 2006; *Grabiec et al.*, 2011; *Sold et al.*, 2013]. Combinations of meteorological and topographic factors broadly control these patterns, although the relative importance of these factors varies widely in space and time [*Grabiec et al.*, 2011]. Atmospheric circulation, precipitable water, air pressure, air temperature, wind speed and direction, elevation, slope exposure, presence of orographic barriers that channelize airflow, surface slope, surface aspect, surface roughness, and relief have all been connected to snow accumulation distribution [*Winstral et al.*, 2002; *Grabiec et al.*, 2011; *Bühler et al.*, 2015].

Snow cover has been mapped from space for more than a half century; however, quantifying snow water equivalent (SWE, a measure of the volume of water) from space remains challenging [*Dietz et al.*, 2012]. SWE is estimated using (i) in situ probe and/or snowpit point measurements [*Zemp et al.*, 2009], (ii) automated stations (snow pillows (i.e., snow telemetry (SNOTEL) sites in the United States) or precipitation gauges on automatic weather stations), (iii) surface elevation differencing using lidar and photogrammetric derived digital elevation models (DEMs) [*Sold et al.*, 2013; *Bühler et al.*, 2015], (iv) passive microwave remote sensing [*Huffman et al.*, 2007], (v) gridded precipitation or downscaled model outputs [*Jarosch et al.*, 2012], (vi) GPS multipath observations [*McCreight et al.*, 2014], and (vii) ground-penetrating radar (GPR) [*Kohler et al.*, 1997; *Machguth et al.*, 2006; *Sold et al.*, 2013; *Gusmeroli et al.*, 2014; *Okorn et al.*, 2014; *van Pelt et al.*, 2014]. Each method has a unique cost benefit (i.e., detailed point observations but negligible spatial coverage or comprehensive spatial coverage but high uncertainty) that has guided methodological choices in the past.

In Alaska, few direct measurements of large-scale SWE distributions exist, although gravimetry and interpolated climate data (e.g., Gravity Recovery and Climate Experiment and Parameter-elevation Relationships on Independent Slopes Model (PRISM)) both suggest high-accumulation magnitudes and spatiotemporal variability [*Arendt et al.*, 2013; *Daly et al.*, 2008; *Hill et al.*, 2015]. Here we present magnitude and variability estimates for snow accumulation on glaciers located in five Alaskan climate regimes [*Bieniek et al.*, 2012] at the end of the 2012–2013 winter using GPR (Figure 1). We use geostatistical extrapolation methods to produce maps of spatially distributed, end-of-season SWE at each glacier. We assess variability across the

Table 1. Glacier Characteristics and Radar Survey Details

	Area (km^2)	Elevation Range (m asl)	Primary Aspect	Survey Date	Snow Density (kg/m^3)	Density-Velocity (m/ns)	CMP Velocity (m/ns)	Probe Velocity (m/ns)	Mean Velocity[a] (m/ns)
Valdez	136.7	65–2310	SE	14 March	330 ± 36	0.235 ± 0.006	0.216 ± 0.005	—	0.225[b] ± 0.006
Scott	141.1	117–1897	SW	19 March	410 ± 45	0.223 ± 0.006	0.229 ± 0.002	0.202 ± 0.008	0.218 ± 0.005
Taku	671.0	0–2117	SE	5 April	410 ± 45	0.223 ± 0.006	0.233 ± 0.005	—	0.228[b] ± 0.006
Gulkana	17.6	1163–2430	S	20 April	365 ± 40	0.229 ± 0.006	0.226 ± 0.005	0.2155 ± 0.015	0.223 ± 0.009
Eureka	33.8	1126–2615	S	21 April	—	—	—	—	0.223[c] ± 0.009
Wolverine	16.7	426–1635	S	7 May	446 ± 49	0.218 ± 0.007	0.217 ± 0.002	0.193 ± 0.015	0.209 ± 0.008
Eklutna	29.4	542–1980	N	24 May	430 ± 47	0.220 ± 0.006	0.225 ± 0.003	0.202 ± 0.007	0.216 ± 0.005

[a]Mean velocity is the mean of velocity estimates derived from (i) empirical column-average density calculation [*Kovacs et al*., 1995], (ii) common-midpoint surveys, and (iii) least squares regression between snow depth derived by probing and all radar traveltime observations within a 2 m radius of the probe site.
[b]Based on density and CMP only.
[c]Based on Gulkana Glacier velocity.

GoA region, evaluate our results alongside direct winter mass balance (B_w) estimates, and consider sampling strategy for future campaigns.

2. Study Area

During the spring of 2013, we conducted ground- and helicopter-based GPR surveys on seven Alaskan glaciers. Sites were deliberately selected in both maritime and continental settings in order to characterize accumulation variability across numerous climate regimes (Figure 1), as defined by *Bieniek et al*. [2012]. Gulkana and Eureka glaciers are located on the southern flank of the eastern Alaska Range in a continental (cold and dry) climate, classified as the Southeast Interior. Eklutna Glacier is located in the northern Chugach Mountains, at a climate region triple junction (Cook Inlet, Southeast Interior, and Northwest Gulf climates) that is characterized by strong interannual climate variability. Wolverine Glacier is located on the Kenai Peninsula in the Northwest Gulf maritime (warm and wet) climate region, which has the most consistent monthly average precipitation of all climatic regions on the GoA coast. Scott and Valdez glaciers are located in the eastern Chugach Mountains and within the Northeast Gulf climate region. Taku Glacier is located in the Coastal Mountains of southeastern Alaska and is the largest outlet glacier of the Juneau Icefield. The Central Panhandle region is thought to receive some of the highest amounts of precipitation in the state. Our sample of glaciers includes areas that range from ~16 to 670 km^2 and mean glacier elevations from ~800 to 1800 m above sea level (asl; Table 1) [*Pfeffer et al*., 2014].

Many of these glaciers have preexisting field programs allowing for validation opportunities and long-term significance. Gulkana and Wolverine glaciers are both part of the U.S. Geological Survey (USGS) Alaska Benchmark Glacier Program where direct and geodetic measurements of mass balance have occurred since the mid-1960s [*O'Neel et al*., 2014]. Alaska Pacific University maintains a mass balance program at Eklutna Glacier [*Sass et al*., 2009] and the Juneau Icefield Research Program measures mass balance at Taku Glacier each year [*Pelto et al*., 2013]. In situ observations are taken at Eureka Glacier for a baseline hydrology study by the Alaska Division of Geological and Geophysical Surveys (DGGS) for the proposed Susitna-Watana Hydroelectric Project, while observations are made at Valdez Glacier as part of a Prince William Sound hydrological modeling study led by DGGS and University of Alaska Fairbanks.

End-of-winter snow accumulation during 2012/2013 was average to above average across Alaska [*Weller*, 2013]. SNOTEL stations closest to our seven study sites (on average ~40 km distant) ranged from −5% to +35% of the long-term median for these individual sites. The highest rates of precipitation occurred during January, with a second pulse during middle to late April. In a more typical year the highest rates of precipitation coincide with the onset of winter and progressively taper off as the season progresses [*Bieniek et al*., 2012]. Our results characterize the spatial distribution of SWE during a single winter and the degree to which the large-scale patterns we identify vary from year to year remains unknown.

3. Methods

We describe the five main steps necessary to convert measured one-way radar wave traveltime (t) along survey profiles to end-of-season distributed SWE for each glacier. These include (i) acquisition of GPR and

ground truth data, (ii) calculation of glacier-specific densities and radar velocities, (iii) calculation of snow thickness and initial SWE estimates along surveyed profiles, (iv) estimation of a postsurvey accumulation correction for each glacier, and (v) application of multiple linear regression models to extrapolate SWE across the entire glacier area.

3.1. Radar Data Collection and Processing

Common-offset GPR surveys were conducted with a 500 MHz Sensors and Software Pulse Ekko Pro system. Surveys were completed in the middle-to-late spring prior to the onset of surface melt, but near the time of maximum end-of-winter SWE. Doing so enabled us to avoid biases in our observations due to the strong influence of melt water on radar wave propagation velocity [*Bradford et al*., 2009] and penetration within the snowpack [*Gusmeroli and Grosse*, 2012]. Although we allowed flexibility in adjusting GPR parameters to changing conditions, typical recording parameters included a waveform-sampling rate of 0.2 ns, a 200 ns time window, and "Free Run" trace increments, where samples are collected as fast as the processor allows, instead of at uniform temporal or spatial increments.

We used several data collection platforms, including a plastic sled towed behind either a snowmobile or a researcher on skis. At Eureka, Scott, and Valdez glaciers, we also surveyed from a helicopter, which was flown 15–40 m above the glacier surface at a velocity of 55–70 km/h [*Gusmeroli et al*., 2014]. Snowmobile data collection dominated, and attention was paid to maintaining a near-constant velocity of 15 km/h. Field parties collected radar profiles along each glacier centerline, and whenever possible, along profiles perpendicular to flow. Data collection in tributaries occurred as time and safety allowed (Figure 2). Logistics only allowed for a limited survey of Taku Glacier, but despite the reduced data coverage, we include results as appropriate to provide insight into the Central Panhandle climate regime.

Coincident GPS data were primarily collected with a Novatel Smart-V1 GPS receiver (Omnistar corrected, L1 receiver with root-mean-square accuracy of 0.9 m [*Pérez-Ruiz et al*., 2011]). A dual-frequency (L1/L2) Topcon GRS-1 Global Navigation Satellite Systems receiver was used at Eureka and Valdez glaciers.

Radargrams were processed using the ReflexW-2D software package (Sandmeier Scientific Software). All radargrams were corrected to time zero, taken as the first break in the first wavelet [*Yelf and Yelf*, 2006], and a dewow filter was applied. When reflectors from the base of the seasonal snow cover were insufficiently resolved, gain and band-pass filters were subsequently applied. Layer picking was guided by ground truth efforts but done semiautomatically using a phase-following layer picker and a simple algorithm that removed obvious mispicks. The seasonal layer was picked at the top of the corresponding wavelet. In the ablation zone, the seasonal layer can be determined with minimal uncertainty; however, in the accumulation zone, numerous reflectors, originating from both within the annual layer and from previous annual layers in the firn below, can create ambiguity in tracing the correct reflector. Both point observations (snowpit/cores; Figure 3a) and line crossovers were used to ensure consistency in choosing the annual layer throughout the accumulation zone (Figure 3b).

Common-midpoint (CMP) surveys were collected with the same antennas in the accumulation zones at most glaciers as an independent estimate of radar velocity. During CMP collection, the transmitting and receiving antennas were progressively separated by 10 cm from a central point. During this process, the traveltime, $t(x)$, of energy reflected from a subsurface interface is described by the normal moveout (NMO) equation:

$$t(x) = \sqrt{t_0^2 + \frac{x^2}{V_{\mathrm{NMO}}^2}}, \tag{1}$$

where x is the antenna separation, t_0 is the zero-offset traveltime, and V_{NMO} is normal moveout velocity. In the case of a homogeneous isotropic layer, equation (1) is exact and V_{NMO} is the radar wave velocity in the medium. For a multilayer case (e.g., a stratified snowpack), refraction across interfaces introduces nonhyperbolic terms and equation (1) is approximate. For small-velocity contrasts, isotropic layers and short-spread conditions (i.e., x approximately equal to reflector depth z) [*Taner and Koehler*, 1969], velocities for each layer can be obtained by substituting V_{NMO} into Dix's equation [*Dix*, 1955].

$$V_i^2 = \frac{V_n^2 \ t_n - V_{n-1}^2 \ t_{n-1}}{t_n - t_{n-1}}, \tag{2}$$

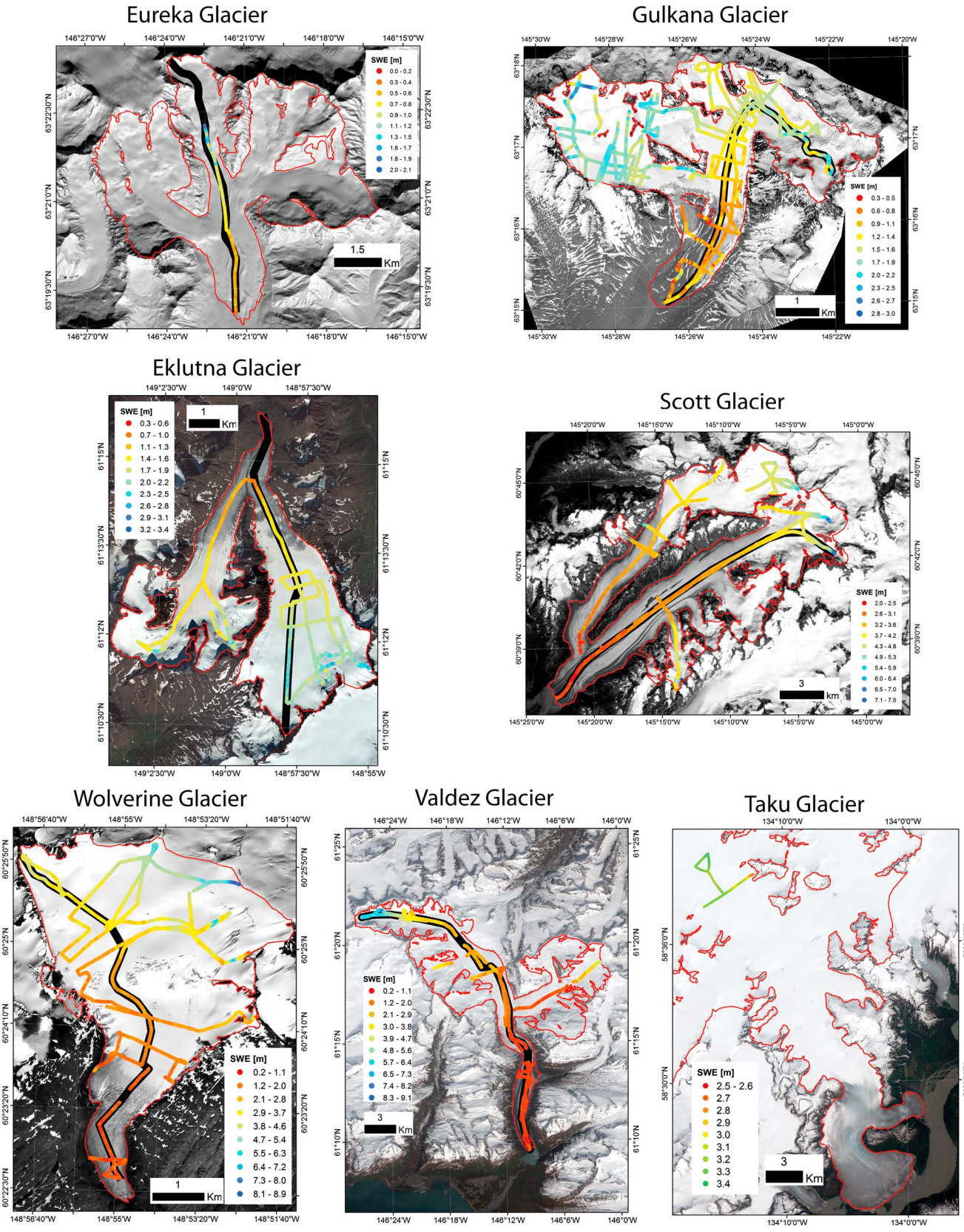

Figure 2. End-of-season SWE at seven glaciers (glacier outlines in red). Heavy black lines indicate centerline profiles that were analyzed on each glacier. Note different spatial and SWE magnitude scales.

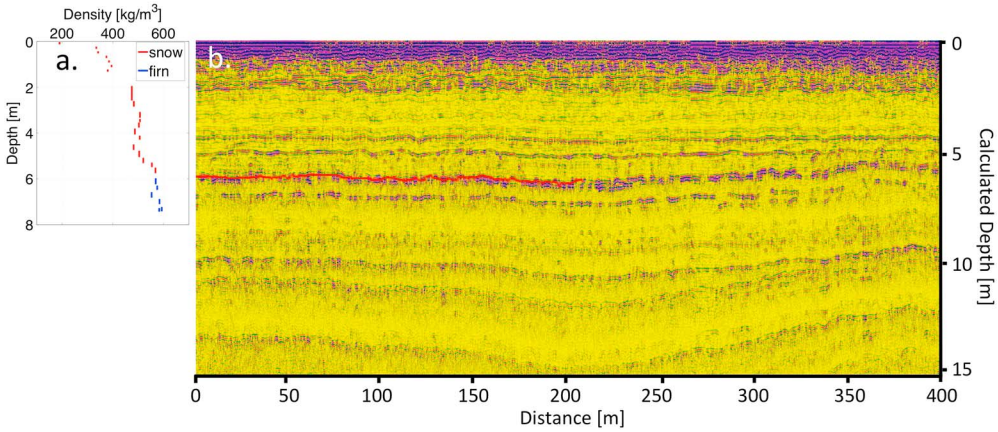

Figure 3. (a) Density profile from snowpit-core in the accumulation zone of Wolverine Glacier. (b) Radargram originating from the core site at 0 m on the *x* axis. Red line notes reflector that was determined to be the annual layer. The bright layers from late-fall rain (section 5.4) are clearly visible above the annual layer.

where V_n is the normal moveout velocity for the *n*th layer and t_n is the zero-offset arrival time corresponding to the *n*th reflection.

We estimated V_{NMO} using coherence statistics [*Sheriff and Geldart*, 1999; *Booth et al*., 2010, 2011, 2013] and corrected all V_{NMO} estimates to account for the systematic slow bias inherent to this method [*Booth et al*., 2010].

3.2. Ground Truth Data Collection

We collected extensive ground truth data to validate common-offset surveys. On most glaciers, we probed snowpack thickness every ~500 m along-track in the ablation zone. Probing was discontinued at the elevation in the accumulation zone where the previous summer surface could no longer be determined confidently (typically when snow depth exceeded ~4 m). On each glacier other than Eureka, one to four snowpits (or pit-core combinations if depth $>$3 m) were excavated to the previous summer surface, which in the ablation zone is marked by the transition from snow (or superimposed ice) to old ice, and in the accumulation zone by the presence of a distinct dust layer, often in conjunction with changes in density and crystal size/shape. Superimposed ice was not observed in any of the snowpits, so it is unlikely it was widely distributed in 2013. We sampled snow and estimated density at 20–50 cm intervals in each snowpit. Cores were extracted with a 7.25 cm diameter core barrel, and a representative sample (~10–25 cm) from each core interval was isolated for density determination. We calculated a density profile and column-average density, ρ, at each site and recorded total snow depth as an additional snow thickness validation point (Table 1).

3.3. Calculation of Snow Water Equivalent

SWE was calculated as the product of one-way radar traveltime, radar wave speed and snow density:

$$\mathrm{SWE} = t v_s \rho. \tag{3}$$

We made three estimates of the radar velocity in snow, v_s, at each glacier: (i) CMP surveys, (ii) empirical column-average density calculation [*Kovacs et al*., 1995], and (iii) least squares regression between snow depth derived by probing and all radar traveltime observations within a 2 m radius of the probe site (Table 1). The average of the three estimates was used to solve for SWE to minimize any potential elevation or spatial density-velocity biases that may exist among these methods.

3.4. Variability and Normalization Methods

Data collection was governed by time, weather, safety, and logistics. As a result, glacier-to-glacier coverage was far from uniform (Figure 2), but a primary goal of our analyses is to evaluate SWE variability at several length scales across each glacier and among the seven glaciers. We minimized biases related to differences in sampling coverage by limiting all analyses of variability to data collected along centerline profiles (black lines on Figure 2) [*Kienholz et al*., 2014].

Table 2. SNOTEL/Weather Stations Specifics and End-of-Season Corrections

	Station Org	Station ID	Station Elevation (m)	Elevation Difference (m)[a]	SWE (cm) (Survey Date)	SWE (cm) (Total)	Correction
Valdez	USDA/NRCS	1055	553	761	40.9	60.5	32%
Scott	USDA/NRCS	1035	428	461	116.6	168.7	31%
Taku	USDA/NRCS	1001	259	1009	212.3	281.2	25%
Gulkana	USGS	15478038	1480	333	80.9	95.3	16%
Eureka	USGS	15478038	1480	407	80.9	95.3	16%
Wolverine	USGS	15236895	990	216	56.6	60.0	6%
Eklutna	USDA/NRCS	1103	469	977	117.9	118.4	1%

[a]Elevation differences are relative to area-weighted mean glacier elevations. USDA: U.S. Department of Agriculture; NRCS: Natural Resources Conservation Service.

At the shortest length scales (10^0–10^1 m) we evaluated the standard deviation of SWE within 5 m elevation bins. Over characteristic surface slopes of 5–10°, these bins span lateral distances of ~30–55 m. Over longer length scales (10^1–10^2 m), we first removed the mean SWE elevation gradient before estimating variance as a function of distance. We assess variance by calculating the mean difference between individual observations and all other observations in discrete 10 m bins up to 500 m from the observation. For each discrete bin, the uncertainty bounds are equal to the standard deviation of all differences in the bin. Over interglacier length scales (10^4–10^5 m), we used the distance from the open coast to the glacier terminus as a moisture source proxy. We chose to use the outermost coastline (i.e., Gulf of Alaska boundary) rather than the shortest distance to the ocean (i.e., smaller sounds and bays) as the topography on outer islands/peninsulas influences storm track, wind fields, and precipitation patterns [*L'Heureux et al.*, 2004; *Bieniek et al.*, 2012].

We also employ a number of normalization methods in our analyses. To examine the relative variability of SWE across an individual glacier, we normalize by the mean SWE of each elevation bin. To compare results between glaciers, we normalize each point by the glacier's elevation range, such that the normalized elevation, z_{norm}, is

$$z_{norm} = (z - z_{min})/(z_{max} - z_{min}), \quad (4)$$

where z is the surface elevation at a point (meters asl) and z_{min} and z_{max} are the minimum (terminus) and maximum (head) elevations of the glacier, respectively [*Arendt et al.*, 2006].

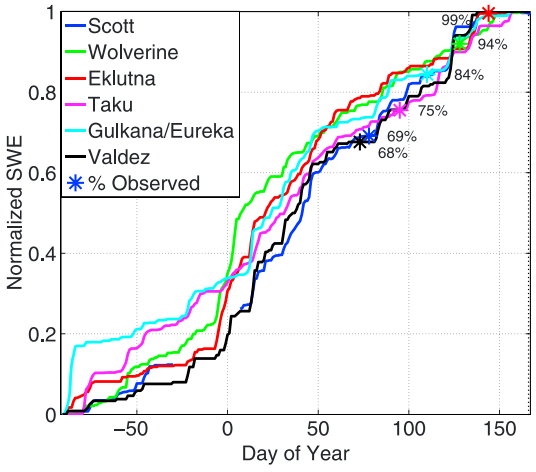

Figure 4. Normalized SWE curves at mean elevation of individual glaciers based on observations from proximal SNOTEL station/AWS with snow/rain partition calculated using moist adiabatic lapse rate. To ensure common comparison across all glaciers, observed SWE values at each glacier are scaled by the ratio between the derived SWE on the day of the survey and the peak derived SWE for the year.

3.5. Temporal and Spatial Extrapolation

Interglacier comparisons require that SWE observed on variable sampling dates be adjusted to the end-of-winter SWE maximum. We use temperature and precipitation records from nearby SNOTEL sites or weather stations (Table 2) to reconstruct a SWE time series at the area-weighted mean elevation of each glacier. The temperature time series was adjusted by applying a moist adiabatic lapse rate (−5°C/km) to the elevation difference between the station and glacier (Table 2). A simple temperature threshold (+1.5°C) [*Dai*, 2008] determined if precipitation fell as snow. Although this correction had a small impact on the adjusted SWE time series, it was necessary to account for early fall storms, during which rain fell at the low-elevation stations, but where temperatures at the glacier's mean elevation implied snow accumulation. Radar-observed SWE was subsequently scaled by the ratio of SWE on the date of the GPR survey in the elevation-adjusted time series to the end-of-winter SWE maximum in the SWE time series (Figure 4).

Table 3. Digital Elevation Model Specifics

	Date	Original Resolution	Source
Valdez	2007	5 m	IfSAR[a]; www.gina.alaska.edu
Scott	2012	5 m	IfSAR; www.gina.alaska.edu
Gulkana	June 2009	5 m	Satellite photogrammetry, USGS
Eureka	2010	5 m	IfSAR; www.gina.alaska.edu
Wolverine	September 2008	5 m	Satellite photogrammetry, USGS
Eklutna	September 2010	2.5 m	Lidar, USGS; http://lidar.cr.usgs.gov/

[a]IfSAR, interferometric synthetic aperture radar.

Extrapolating SWE from point measurements to the basin scale has been a topic of focused research for decades [*Woo and Marsh*, 1978; *Balk and Elder*, 2000; *Molotch et al*., 2005]. Most commonly, the dependent variable SWE is related to a series of explanatory terrain parameters thought to influence its distribution. At the six glaciers with sufficient data coverage (including Eureka Glacier, despite only centerline coverage), we extrapolated radar-observed SWE over the entire glacier area. We use the extrapolated fields to calculate glacier-wide total SWE (B_w; km^3 water equivalent (we)) and mean specific (area-averaged) winter balance ($\overline{B}_w$; mwe). End-of-season SWE elevation gradients presented here are consistent with winter mass balance (b_w) gradients. Glacier area and boundaries from the Randolph Glacier Inventory [*Pfeffer et al*., 2014] were modified slightly in accordance with recent high-resolution satellite imagery.

We used a multiple linear regression model of the form,

$$\mathrm{SWE}_{(i,j)} = c_1 x_{1(i,j)} + c_2 x_{2(i,j)} + \ldots + c_n x_{n(i,j)} + \varepsilon_{(i,j)}, \tag{5}$$

where $\mathrm{SWE}_{(i,j)}$ is the predicted value at location i,j; c_1, c_2, and c_n are the coefficients of the model; x_1, x_2, and x_n are independent variables related to surrounding terrain and processes; and ε is the residual. We applied the regression model stepwise and set a threshold for inclusion of an independent variable as a change in $r^2 > 0.001$. To avoid redundancy in the independent variables (multicollinearity), we employ a secondary threshold such that if the variance inflation factor exceeded 4, the variable was not included [*Montgomery et al*., 2001]. Terrain parameters were derived from 10 m DEMs (Table 3) and included surface elevation, surface slope, surface curvature, aspect, northness [*Molotch et al*., 2005], and wind exposure/shelter (*Sx*; Figure 5) [*Winstral et al*., 2002].

Aspect (orientation of the surface) and slope (first derivative of the surface) were calculated by fitting a plane to a 3×3 cell window around the primary elevation cell. Curvature (second derivative of the surface) was calculated by fitting a plane to a 3×3 cell window around the primary slope cell. Aspect was transformed to -1 (south) to 1 (north) by taking the cosine of the original value. Northness is a solar radiation parameter that becomes increasingly relevant during spring [*Revuelto et al*., 2014], but even during the accumulation season, this parameter may reflect differences in snow metamorphism processes and/or location of sun crusts, which can influence wind redistribution. Northness is estimated as the product of the cosine of aspect and sine of slope. It is bounded at -1 by steep, south facing slopes and at +1 by steep, north facing slopes. Flat surfaces yield 0.

Wind exposure/shelter, *Sx*, is calculated at each point as:

$$Sx_{\alpha,d\,\max}(x_i, y_i) = \max\left(\tan^{-1}\left\{ \frac{z(x_v, y_v) - z(x_i, y_i)}{\left[(x_v - x_i)^2 + (y_v - y_i)^2 \right]^{1/2}} \right\} \right), \tag{6}$$

where α is the azimuth of the search direction, *d*max the search distance, and (x_v, y_v) are the set of all grid points along the line defined with α and within *d*max. Rather than prescribing a dominant wind direction based on distal and/or geographically biased AWS observations and therefore likely mischaracterizing the effects of wind redistribution, we calculate *Sx* at 5° azimuth increments for *d*max distances of 100, 200, and 300 m [*Molotch et al*., 2005; *Schirmer et al*., 2011; *Revuelto et al*., 2014]. We include the *Sx* combination (i.e., α and *d*max) in the final regression analysis that had the highest correlation to observed SWE. Importantly,

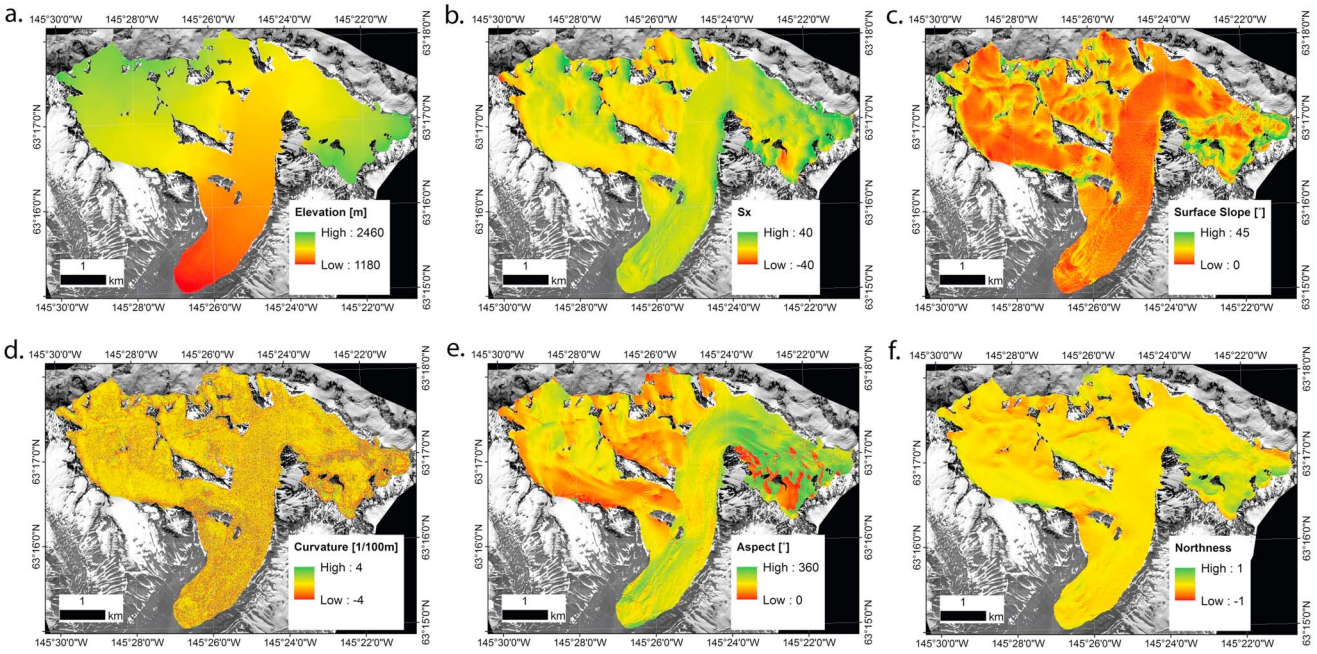

Figure 5. Example of derived terrain parameters used in multiple regression analysis for Gulkana Glacier. (a) Elevation, (b) *Sx*, (c) surface slope, (d) curvature, (e) aspect, and (f) northness.

terrain parameters are proxies for physical processes (i.e., *Sx* is a proxy for snow deposition due to wind redistribution) and do not capture the underlying physics of said process.

Site-specific regression coefficients were applied to DEM raster fields as a first estimate of SWE across the glacier area. We tested the residuals of each multiple linear regression model for normality (Moran's $I > 0.65$, $p > 0.001$). In each case, model residuals were normally distributed and had high spatial autocorrelation; the latter suggesting that physical processes, not captured by the terrain parameters, exerted control on the final SWE distribution. We produced additional raster fields of extrapolated residuals in order to represent these physical processes [*Carroll and Cressie*, 1996; *Balk and Elder*, 2000; *Erxleben et al.*, 2002; *Molotch et al.*, 2005]. We produced the final spatially distributed SWE field by adding the residuals back to the regression output. To test the sensitivity of the regression results to data coverage, the regression model was run using all available radar data from each glacier as input, as well as using only centerline observations to estimate B_w. We also estimated B_w by integrating the centerline-only SWE gradient over the glacier hypsometry (hereafter called hypsometric estimate), which more closely approximates the methods used by traditional mass balance programs [*Van Beusekom et al.*, 2010].

3.6. Additional Data Sources

We used 2 km PRISM monthly norms (1971–2000) [*Daly et al.*, 2008] for temperature and precipitation forcing. PRISM fields are built using local regressions between weather station data and topographic variables. Most weather stations are located at low-elevation in Alaska, and hence, many PRISM grid cells rely on significant extrapolation to high-elevation terrain. At each glacier, we estimated the fraction of total precipitation that fell as snow on the basis of whether the monthly mean temperature exceeded 1.5°C. With this simple threshold approach, we find that the accumulation season for most glaciers was from September through May, except at Wolverine Glacier (October to March) and Scott Glacier (October to May).

The USGS Benchmark Glacier Program has made biannual mass balance measurements on Gulkana and Wolverine glaciers since the mid-1960s [*O'Neel et al.*, 2014]. USGS calculates glacier-wide seasonal (B_w and B_s) and annual balances (B_a) from stake and pit measurements made at fixed locations. A geodetic correction, derived from DEM differencing over multiyear intervals, is applied to the cumulative annual mass balance, but not to seasonal balances. These measurements provide an opportunity for comparing radar-derived winter balance estimates to those derived from the glaciological method.

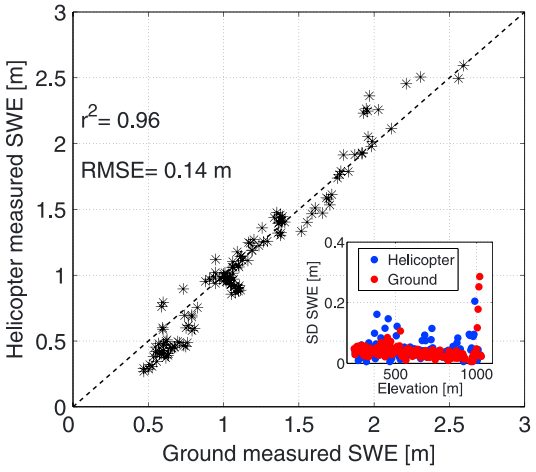

Figure 6. Comparison of helicopter- and ground-measured SWE (as mean of 5 m elevation bins) along the east branch of Scott Glacier. Inset: standard deviation of SWE in 5 m elevation bins as a function of elevation for each system.

4. Results

4.1. Material Properties

Glacier-averaged mean snow densities ranged from 330 ± 36 kg/m^3 at Valdez Glacier to 447 ± 49 kg/m^3 at Wolverine Glacier, with the mean of all six sites being 399 ± 44 kg/m^3. We found limited sensitivity of the column-average density to lower density surface snow, while at Gulkana and Wolverine glaciers, where numerous (~4 per glacier) snowpits/cores were excavated, column-average density did not exhibit coherent spatial or elevation dependencies [*Jonas et al.*, 2009]. Accordingly, we calculate a single depth-invariant radar velocity based on the mean column-average density for each glacier. This empirical calculation is subsequently averaged with the CMP and probe-derived velocities at each glacier. The mean radar velocity for all seven sites was 0.218 ± 0.006 m/ns, with a range from 0.209 ± 0.008 m/ns at Wolverine to 0.225 ± 0.006 m/ns at Valdez (Table 1). Across all glaciers, the probe method resulted in the slowest mean velocity (0.203 ± 0.011 m/ns), while the density relation resulted in the highest mean velocity (0.225 ± 0.006 m/ns).

4.2. Collection Platform

There is a potential for biases between the different collection platforms. The ground and airborne platforms we used had substantially different travel speeds (hence trace density) and footprint size at the annual layer interface. To detect potential biases, we designed a direct comparison between the two methods along the

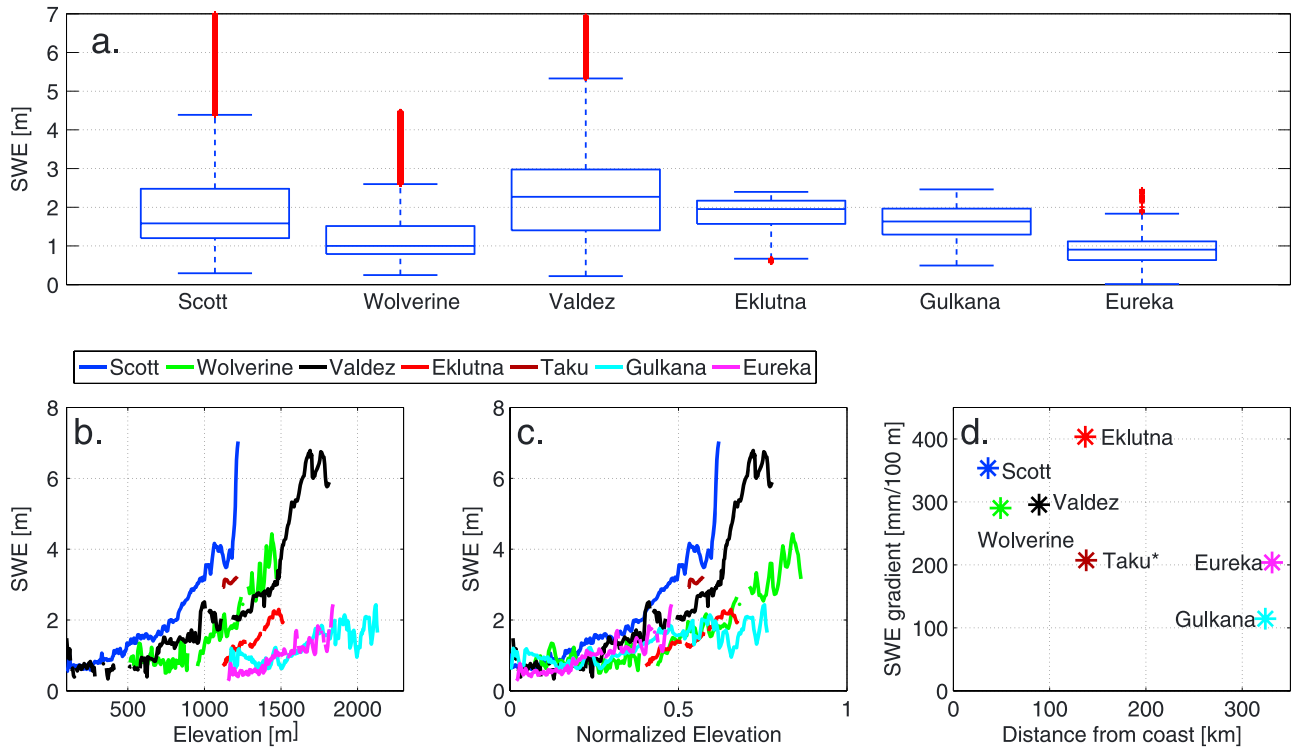

Figure 7. (a) Boxplot of SWE along glacier centerlines, with center mark indicating the median, the edges of the box are the interquartile range (IQR), and whiskers extend to 1.5 IQR. Red stars are outliers. (b) Mean SWE (in 5 m elevation bins) as a function of elevation, (c) mean SWE as a function of normalized elevation, and (d) SWE elevation gradients as a function of Distance from Coast. Asterisk indicates that only limited elevation range was surveyed.

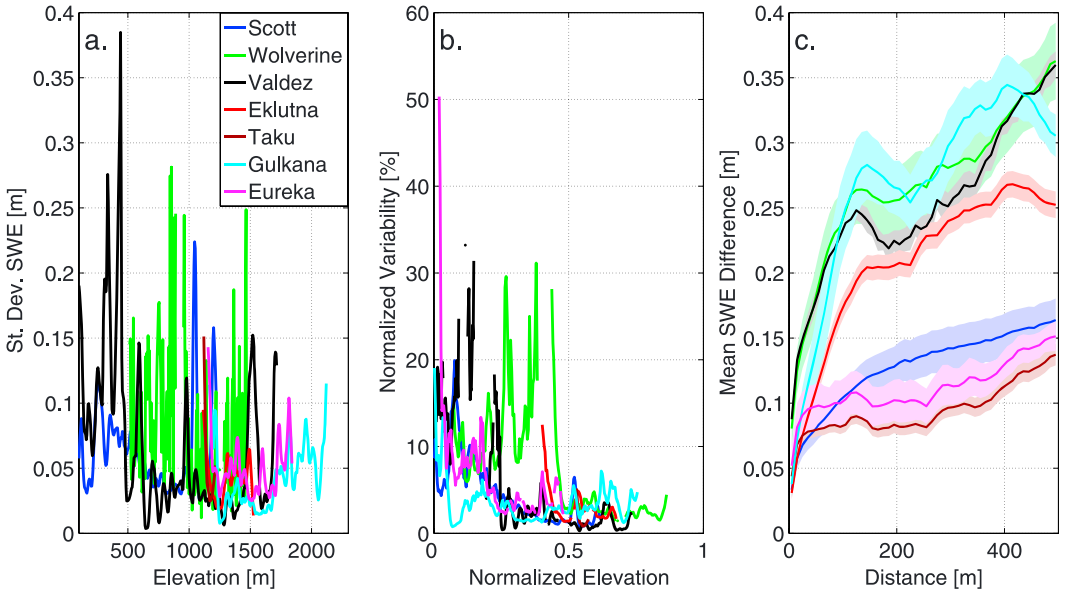

Figure 8. (a) Standard deviation of SWE observed along glacier centerlines in 5 m elevation bins as a function of elevation, (b) standard deviation of SWE normalized by mean SWE in 5 m elevations bins as a function of normalized elevation, and (c) mean difference in SWE between each observation and all observations as a function of distance (calculated in 10 m distance bins). Bounds are the standard deviation of this difference (scaled by 50% to improve visibility) as a function of distance.

east branch centerline of Scott Glacier. Although we made efforts to align the two ground tracks, 10–50 m offsets were common, and SWE differences integrate both physical (due to survey offsets) and methodological differences (due to sensor footprint, survey speed). We find that mean SWE, binned at 5 m elevation intervals, is largely independent of acquisition method both in magnitude (coefficient of determination, $r^2 = 0.96$, root-mean-square error (RMSE) = 0.14 m) and variability (root-mean-square error (RMSE) = 0.04 m, Figure 6) and thus are confident that the data sets can be used interchangeably.

4.3. SWE Magnitude and Variability on Glacier Centerlines

After applying the common-date adjustment that ranged from 1 to 30% (Figure 4 and Table 1), we compared the magnitude and variability across the six glaciers with significant spatial coverage. Median SWE ranged from 0.90 m to 2.27 m (Figure 7a), with the broadest range at Valdez and smallest range at Eklutna Glacier. At all glaciers, SWE exhibits strong elevation dependence, with linear gradients ranging from 115 mm/100 m to 400 mm/100 m (Figure 7). The SWE gradient decreases by ~60 mm/100 m per 100 km from the coastline (Figure 7d).

To assess spatial variability over short length scales (30–55 m) on individual glaciers, we calculated the standard deviation of all observations in 5 m elevation bins (i.e., 100–105 m asl). Eklutna Glacier exhibited the smallest variability (0.04 m) and Wolverine Glacier the largest (0.08 m; Figure 8a). At all glaciers variability in the ablation zone exceeded that in the accumulation zone. This is particularly evident when assessed as relative variability (i.e., normalized by mean SWE of that elevation bin) (Figure 8b). Over length scales of hundreds of meters, two distinct patterns emerge: (i) four glaciers (Gulkana, Wolverine, Eklutna, and Valdez) exhibit a rapid increase in variability over the first ~150 m, with a slow increase in variability beyond, and (ii) three glaciers (Scott, Eureka, and Taku) exhibit a gradual increase in variability over the entire distance range that the calculation was performed over (Figure 8c).

4.4. SWE Regression

We tested a suite of explanatory terrain parameters for inclusion in a regression model at six glaciers with sufficient data coverage (including Eureka, despite it only having centerline coverage, but excluding Taku). Parameters that significantly and independently increased the explanatory ability of the model were included, and we allowed for variable parameter suites among the glaciers. Elevation dominated the explanatory ability at all sites (Table 4). Wind exposure/shelter, *Sx*, is the only other independent term

Table 4. Standardized Regression Coefficients Relating SWE to Terrain Parameters[a]

	Scott	Wolverine	Valdez	Eklutna	Eureka[b]	Gulkana
Elevation	0.810	0.909	0.797	0.750	0.741	0.585
Sx	0.203	0.260	0.190	−0.294	0.178	−0.074
Slope	—	0.159	−0.090	—	—	0.277
Curvature	—	—	—	−0.077	—	—
Aspect	—	—	0.047	0.093	—	—
Northness	0.172	0.030	—	−0.414	—	—
r^2	0.76	0.69	0.70	0.58	0.81	0.44
RMSE (m)	0.49	0.79	0.84	0.25	0.17	0.32
r^2 with residuals	0.98	0.98	0.98	0.94	0.94	0.98
RMSE with residuals (m)	0.13	0.20	0.18	0.09	0.11	0.06

[a]Only those terrain parameters with regression coefficients were used in the final models.
[b]Eureka is included here although data collection only consisted of a centerline profile.

included in all six regressions and is the second strongest term in four of these (Table 4). *Sx* lag distances were 100 m at Scott and Eklutna, 200 m at Gulkana and Valdez, and 300 m at Eureka and Wolverine, with wind azimuths that were split between east and southeast and west and northwest. Additional terms were included at five of the six glaciers, with the largest contributions from slope and northness (Table 4). Measured and predicted SWE agree well, with r^2 between 0.44 and 0.81, suggesting that the site-specific regression models perform reasonably well (Table 4). However, adding the spatially extrapolated residuals

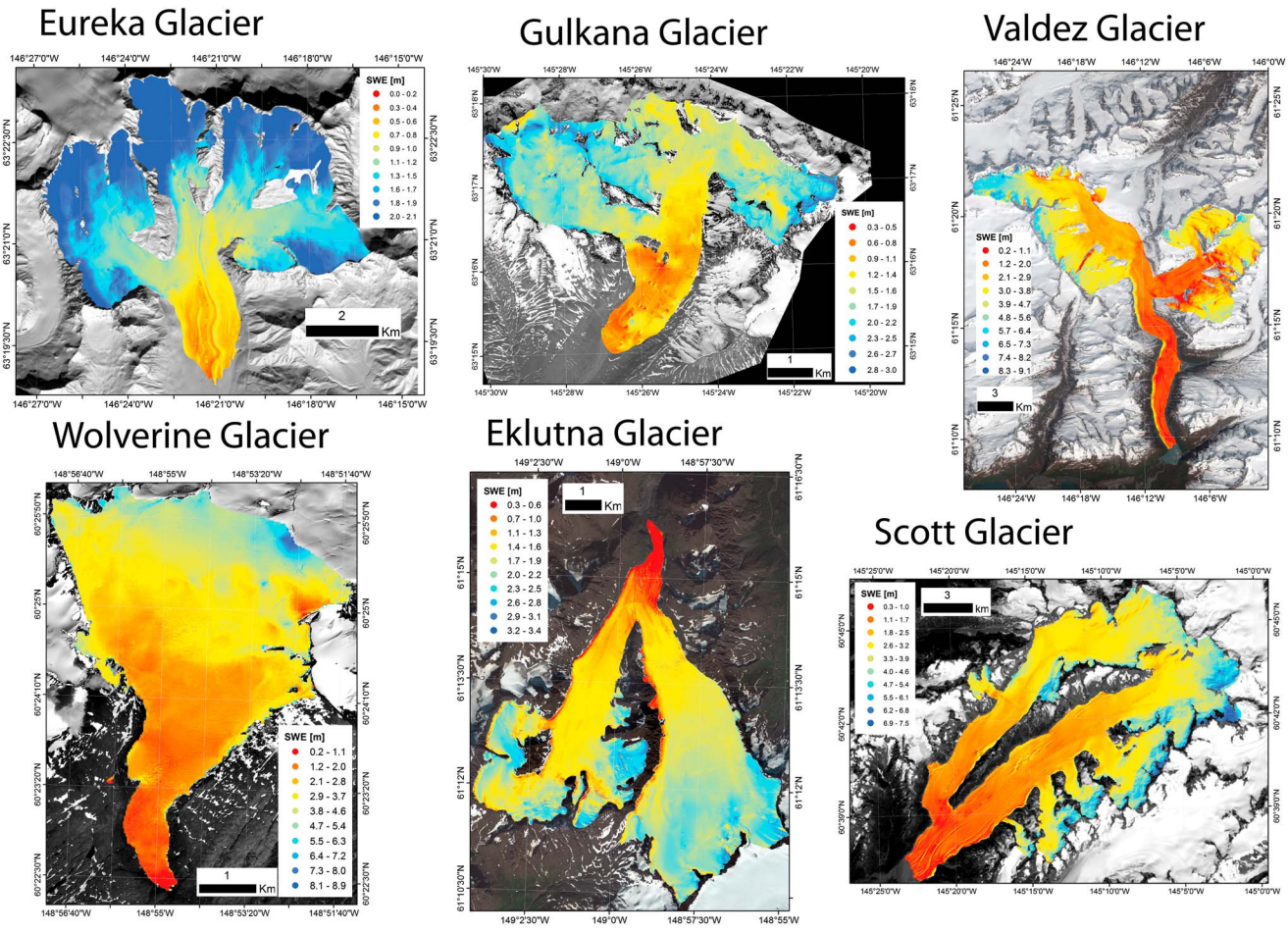

Figure 9. End-of-season distributed SWE at six glaciers throughout Gulf of Alaska region. Radar-observed SWE on survey tracks is overlaid for comparison. Both variables are plotted on the same color scale within each subplot, although each glacier has a different scale to show the basin-scale variability.

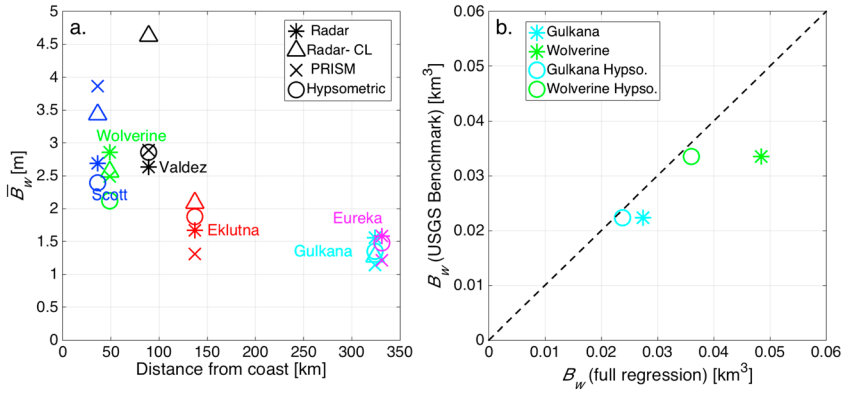

Figure 10. (a) Mean SWE (b_w) values at six glaciers from full radar-derived regression results (asterisk), centerline-only (CL) regression results, climatological mean PRISM SWE values (cross), and hypsometric regression (circle). (b) Scatterplot of total SWE (B_w) derived from USGS stake networks and from full radar-derived regression results (asterisk) and a hypsometric regression (circle).

back in significantly improves model agreement ($r^2 = 0.94$ to 0.98), suggesting that the parameters used here do not capture all processes that produce the high spatial variability of SWE in complex topography (Figure 9). The mean specific winter mass balance $(\overline{B}_w)$ calculated from the distributed SWE fields ranged from 1.56 m at Gulkana to 2.85 m at Wolverine (Figure 10a and Table 5) and collectively exhibited a decreasing value with distance from the coast, similar to SWE elevation gradients (Figure 7d).

4.4.1. Implications of Nonuniform Data Acquisition

Logistical constraints (crevasses, weather, and resources) often prohibit uniform data acquisition on glaciers. We assessed the influence of profile coverage on $\overline{B}_w$ by calculating this value in two additional ways, including a multiple linear regression analysis using only the centerline observations and also by integrating the centerline SWE elevation gradient over the glacier hypsometry. Hypsometric estimates for $\overline{B}_w$ differed by $<$1% to 30% from the full multiple linear regression values of $\overline{B}_w$ (Figure 10a). However, when B_w values from each glacier were collectively summed, the estimates differ by only 3% between these methods. In contrast, the summed B_w estimate from the centerline-only regression differs by ~35% from the full coverage regression estimate.

4.5. Comparison to Other Estimates

We compare total (B_w) and area-averaged $(\overline{B}_w)$ winter balance to two independent estimates, the first extracted from the PRISM data set and the second calculated from direct measurements of the USGS mass balance program. The PRISM values retain the overall spatial pattern of decreasing SWE with distance from the coast (Figure 10a). At both Scott and Valdez glaciers, PRISM exceeds radar-derived values by 9–36%, while at the four other sites PRISM underestimates the radar values by 13–30% (Figure 10a). Broadly speaking, the misfit exhibits a spatial pattern such that PRISM exceeds the radar estimate at the maritime glaciers, while the radar estimate exceeds PRISM for the continental glaciers. There is reasonable agreement between B_w estimates derived from radar and glaciological methods at both Gulkana and Wolverine glaciers, with 6–20% difference and 7–36% difference, respectively. At both glaciers, the agreement is better with the hypsometric estimate than the full multiple linear regression model estimate.

Table 5. Glacier-Wide (B_w) and Area-Averaged SWE $(\overline{B}_w)$

	B_w (km^3)	B_w CL (km^3)[a]	B_w Hypso. (km^3)	$\overline{B}_w$ (m SWE)	$\overline{B}_w$ CL (m SWE)[a]	$\overline{B}_w$ Hypso. (m SWE)
Valdez	0.3547	0.6170	0.3815	2.63	4.63	2.83
Scott	0.3776	0.4829	0.3372	2.69	3.43	1.89
Taku	—	—	—	—	—	—
Gulkana	0.0275	0.0224	0.0238	1.56	1.27	1.35
Eureka	—	0.0538	0.0502	—	1.58	1.48
Wolverine	0.0484	0.0434	0.0360	2.85	2.56	2.12
Eklutna	0.0504	0.0627	0.0565	1.67	2.09	1.66

[a]CL: centerline-only.

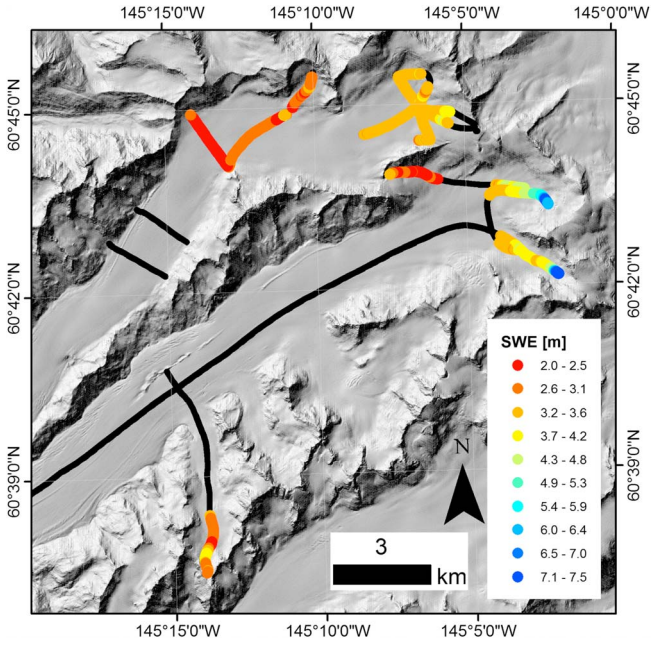

Figure 11. SWE on Scott Glacier in elevation band 1000–1300 m. Black lines note other radar transects outside this elevation range.

5. Discussion

We collected GPR data at seven glaciers in five climate zones throughout Alaska during the spring of 2013, a climatologically average year [*Weller*, 2013]. We used probes, snowpits, and CMPs to calculate snow density and radar velocity, which allowed us to characterize SWE along survey profiles. We developed multiple linear regressions based on terrain parameters to model accumulation over unmeasured portions of the glacier. Finally, we used both the profiles and extrapolated fields to assess the magnitude and variability of SWE over a range of spatial scales, from meters to hundreds of kilometers. Below, we discuss the significance of the multiple linear regression analysis as it applies to both end-of-year SWE and SWE variability.

5.1. Multiple Linear Regression Analysis

Results from the multiple linear regression analyses clearly demonstrate that elevation is the primary explanatory parameter for the distribution of SWE, in agreement with previous studies looking at seasonal snow cover over large elevation ranges [e.g., *Molotch and Bales*, 2005; *Lehning et al.*, 2011]. Wind exposure/shelter (*Sx*), a proxy for local variations in wind speed due to topography, reflects the redistribution of snow by wind [*Winstral et al.*, 2002]. Glaciers with a dominant wind direction (perhaps due to channelized flow during storms) are likely to have SWE distributions strongly influenced by wind redistribution, while this influence would be reduced at glaciers where wind direction is more variable. The influence of wind redistribution is also likely dependent on snow density, as lower density snow would allow for redistribution during postdepositional wind events.

At all glaciers except Eureka, one to three additional parameters had explanatory power in the final regression. The sign and magnitude of these terms varied substantially among the sites, which reduces our confidence in attributing these relationships to physical processes that control SWE distributions. Before adding residuals back into the solution, our analysis yielded coefficients of determination (r^2) comparable to previous studies [e.g., *Revuelto et al.*, 2014]. At all sites, r^2 increased by more than 0.2 with the addition of the residuals field, which both highlights the benefit of this approach and the limitation of terrain parameters at explaining SWE distribution in complex topography [*Erxleben et al.*, 2002; *Grünewald et al.*, 2010; *Lehning et al.*, 2011].

The centerline-only regression analyses highlight a number of important points regarding data collection. Consistently large differences exist between $\overline{B}_w$ calculated via regressions based on the full and centerline-only data sets. This difference is largely attributable to the limited sampling of terrain parameters (i.e., slope, aspect, and *Sx*) in the centerline-only data set relative to the full radar data set and the full distribution of these variables on the glacier. Erroneous $\overline{B}_w$ estimates can occur by applying regression coefficients based on a limited sampling of terrain parameters to the glacier's full distribution (i.e., see Valdez Glacier in Figure 10a). In contrast, estimates of $\overline{B}_w$ from the full regression and hypsometric estimate show close agreement. This agreement emphasizes the strong explanatory power of elevation and a field sampling distribution that typically captures a greater extent of the full distribution relative to any other parameter.

However, simple hypsometric estimates are sensitive to accurately capturing the SWE elevation gradient, which can be strongly influenced by inclusion/exclusion of tributaries. The 1000–1300 m elevation band at Scott Glacier, which includes numerous basins in both branches, provides a clear example (Figure 11).

Large differences in SWE, which range between 1.78 and 7.32 m, with a mean of 3.28 and a standard deviation of 0.77 m, are observed in this elevation range. The SWE gradient using all observations is ~50 mm/100 m lower than that calculated using centerline-only observations. The large differences between these branches illustrate how complex micrometeorological variables (i.e., orientation to storm track or prevailing wind direction) can strongly influence accumulation distribution and the area average, $\overline{B}_w$. Furthermore, it highlights that at certain glaciers, particularly those with complex geometries, measuring SWE along the primary centerline may be insufficient to resolve accumulation patterns (i.e., at the basin scale) pertinent to calculations of B_w over the entire glacier area. Future ground and airborne campaigns would benefit from increased spatial coverage in the accumulation area, as it exhibits a strong control on the SWE elevation gradient and basin-scale variability can be quite large.

We summed B_w across all glaciers using both the full data set regression and hypsometric estimate and found close agreement (~3% difference) between these two approaches. This suggests that accurate regional-scale estimates can be obtained with centerline observations from multiple glaciers. On an individual glacier, centerline-only observations may be sufficient for calculating B_w, but only if the SWE gradient is accurately captured by this profile. Our results show that robust portrayal of the SWE distribution requires broader spatial data acquisition to sample the full distribution of terrain parameters and ensure accurate multiple linear regressions.

5.2. Spatial Variability of SWE

Over the shortest spatial scales (~30–55 m) analyzed, SWE varies by up to 40% of the local mean. The variability and, in particular, the relative variability, is greatest in ablation areas (Figure 8) and decreases at higher elevations. On Scott Glacier, the variability is invariant of collection platform (Figure 6 inset), suggesting that the larger footprint of helicopter-based radar does not create a significant bias in observed variability when analyzed over these spatial scales. Enhanced variability in the ablation zone is consistent with large meter-scale surface roughness from crevasses, supraglacial streams, and moulins that characterize this zone. Wind redistribution of early season snowfall is preferentially deposited in surface depressions, thus smoothing the apparent surface roughness as the winter progresses, although the spatial pattern of the initial roughness is preserved in the end-of-season SWE [*Schirmer et al*., 2011]. The observed variability in the ablation zone suggests that in order to accurately capture snow depth in this zone, one must average numerous sample points over a region approximately 30×30 m. Over these short distances, the highest variability, both in absolute and normalized values, was found in the ablation zones of Valdez and Wolverine glaciers, with the lowest at Taku and Eklutna (Figure 8). The low variability observed at these latter sites may be due to biases introduced by the sampling coverage (i.e., limited to no coverage in the rough ablation zone). However, low variability at Taku is consistent with previous studies [*Pelto and Miller*, 1990], suggesting that higher-density snow and limited wind redistribution may be characteristic of this climate zone.

On the individual glacier scale, elevation provides the dominant control on SWE magnitude (Figures 7b–7d), in part caused by declining air temperatures due to orographic lifting and decreasing saturation pressures [*Roe*, 2005]. The SWE gradients we measured (115–400 mm/100 m) exceed other alpine environments such as the Swiss Alps [*Grünewald and Lehning*, 2011], Intermountain West of the U.S. [*Anderson et al*., 2014], and Svalbard [*Grabiec et al*., 2011] by a factor of 2–3. In part, the steep gradients are a result of characteristically large late-summer and fall coastal Alaska storms [*Bieniek et al*., 2012] that often deposit snow at upper elevations and rain at lower elevations. The steepest and most nonlinear gradients are found closest to the coast where relatively warm water and seasonal cyclogenesis exist. This proximity may result in enhanced quantities of orographic precipitation and a temperate climate, which likely contributes to the frequent occurrence of split snow-rain events throughout the entire year and renders these systems increasingly sensitive to increases in winter temperature.

When orographic forcing (elevation dependence) is removed from the basin-scale analysis of variability two distinct groupings emerge (Figure 8c). However, there is no apparent pattern in defining features (e.g., climate zone, glacier size, geometry, prevailing wind direction, and sampling coverage) explain the group members. Both of these groups exhibit inflection points at lag distances of 50–200 m, which is substantially longer than in the alpine seasonal snow environment [e.g., *Anderson et al*., 2014]. Mountain glaciers appear to have length scales of variability between ice sheets and nonglacierized landscapes reminiscent of the roughness length scale of the underlying terrain.

On a regional scale, distance from the coast, a clear proxy for distance from the primary moisture source, robustly describes $\overline{B}_w$ [*Masson-Delmotte et al*., 2008]. A similar pattern of decreasing SWE with increased distance from the coast is observed in West Antarctica [*Kaspari et al*., 2004] and Svalbard [*Grabiec et al*., 2011]. The GoA is the "graveyard" of Pacific storms; the combination of barotropic and topographic processes limit the inland penetration of storms in Alaska, resulting in strong precipitation gradients [*Mesquita et al*., 2010; *Bieniek et al*., 2012]. This pronounced decrease in accumulation is consistent with other large-scale climate products [*Daly et al*., 2008; *Bieniek et al*., 2012; *Hill et al*., 2015].

5.3. Comparison to Other Winter Mass Balance Estimates

We found reasonable agreement (9–36% differences) between basin-scale PRISM and radar $\overline{B}_w$ estimates, with PRISM generally matching or overestimating $\overline{B}_w$ near the coast and underestimating $\overline{B}_w$ in continental settings. Although the 2012–2013 winter was characterized by average accumulation, a portion of this disagreement may be explained by comparing 30 year climatological means to a specific year. PRISM does not differentiate between rain and snow, and only has monthly resolution, limiting precision in partitioning snow and rain during spring and fall. However, differences between PRISM and radar $\overline{B}_w$ are not proportional to the temperature-constrained accumulation season duration, suggesting that the simple approach we utilize to determine the accumulation season is not the primary cause for these differences. Discrepancies likely arise because the 2 km spatial resolution of PRISM cannot resolve the high spatial variability in accumulation. Nonetheless, our results suggest that GPR offers a new approach for refining PRISM in high-elevation, glacierized terrain where few other observational constraints exist.

We found 6–36% differences between radar and glaciological estimates of B_w at the USGS Benchmark Glaciers [*O'Neel et al*., 2014]. In both cases, GPR suggests a higher accumulation rate than does the glaciological estimate (Figure 10b). Although the simpler hypsometric estimates agree better with the glaciological estimates than the regression approach, we still do not know which is the best estimate of actual accumulation. The discrepancies do, however, provide insight into the potential biases inherent to each method. Stakes are typically installed in open locations away from obstacles where the aspect and slope are broadly representative. In other words, stake locations are chosen to minimize accumulation or melt biases. Unfortunately, GPR profiles reveal elevation-independent centerline variability that results in a strong sensitivity to stake location. For example, changing the location of a stake in the accumulation area of Wolverine Glacier by 30 m in elevation could produce up to a 30% decrease in the SWE gradient. Although the radar can provide more complete areal coverage than a standard stake distribution, imaging both shallow and deep snowpacks across the glacier, sections of the glacier still cannot be sampled well. One potentially large bias arises from the inability to sample crevassed regions (i.e., Figure 2, Wolverine Glacier), which can represent a significant portion of total glacier area for certain glaciers. This sampling bias affects cumulative SWE in an unknown manner.

The cumulative mass balance time series (1967–2013) for Wolverine Glacier is more negative when evaluated geodetically than when direct, but sparse glaciological measurements are used [*Van Beusekom et al*., 2010; *O'Neel et al*., 2014]. A least squares geodetic adjustment suggests that this misfit arises from either overestimating accumulation or underestimating ablation. Although accumulation uncertainty was previously suggested as a driver [*Van Beusekom et al*., 2010], this analysis identifies ablation underestimates as a potential misfit source. The temporal snapshot presented here needs to be evaluated over multiple years to determine the interannual persistence of this relationship.

5.4. Accumulation Zone Radar Stratigraphy

The determination of the annual layer in the ablation zone is generally straightforward, due to the strong density (and hence dielectric constant) differences between seasonal snow and ice. However, in the accumulation zone, numerous reflectors of varying strength and spatial coherence challenge distinguishing the annual layer from previous firn layers or subannual internal reflectors (Figures 3b and 12). This difficulty is exacerbated when storms (often early in the accumulation season) deliver rain over some portion of the glacier's elevation range. The subsequently refrozen granular snow produces a stark density contrast and a strong radar reflector when subsequently buried [*Brandt et al*., 2009; *Gusmeroli et al*., 2014]. In fact, these interfaces may be brighter than the reflector at the base of the annual layer (Figure 12). Furthermore, snow that does fall during these split rain-snow events tends to increase in thickness with elevation, emulating firn

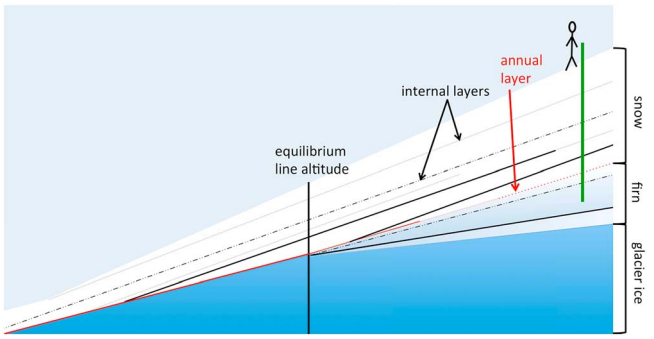

Figure 12. Schematic diagram of seasonal snow stratigraphy on a glacier. Numerous layers/reflectors typically exist both within the seasonal snow and below the summer surface in the firn. The variable line styles are indicative of the relative strength/persistence of such layers. The annual layer, as noted in red, may not be the strongest reflector. Internal layers that emerge in the snow stratigraphy result from storms that deposit rain on the lower glacier. In situ observations high on the glacier (i.e., shallow core) are instrumental for determining the annual layer and following this layer down glacier in the radar stratigraphy.

and further challenging layer interpretation. Figure 12 illustrates how the practice of following reflectors upglacier will miss a potentially significant portion of the annual accumulation. In late fall 2012 across much of the GoA, a warm sequence of storms saturated early season snow with rain well above the equilibrium line altitude. Upon refreezing, this layer had similar density to the firn below (Figure 3a) and, once buried, produced a strong internal reflector. Ground truth observations in late spring showed that the base of the annual layer was located below this rain-saturated snow, at times by a distance of several meters, and was identified by a distinct dust layer and change in grain structure. This interface also produced a radar reflector, but it is likely that without ground truth observations, this layer would not have been correctly identified, causing $\overline{B}_w$ to be underestimated by >50% for some glaciers. Although ground truth observations in the accumulation zone are time intensive and challenging, our results indicate that they are essential to the accurate interpretation of GPR layer stratigraphy (Figures 3 and 12). We caution that the interpretation of GPR data without these constraints, particularly with snowpacks that exhibit a complex stratigraphy, can result in significant accumulation biases.

5.5. Uncertainty Analysis

Previous assessments [*Previati et al.*, 2011; *Sold et al.*, 2013; *Gusmeroli et al.*, 2014] have suggested uncertainties of ±5–16% in determining snow thickness from GPR. At a single point, errors in snow thickness arise due to uncertainty in t (i.e., picking the time zero interface and the annual layer) and the radar velocity, v_s. The conversion to SWE often introduces further uncertainty from simplifying density assumptions, like using a column-average value. The uncertainty in t can be written as:

$$\sigma[t] = (\sigma[t_1]) + (\sigma[t_2]), \tag{7}$$

where t_1 and t_2, represent the surface and annual layer interfaces, which each have an uncertainty of 0.2 ns. As the uncertainties in each term are not independent, the uncertainty for SWE along a radar profile is the sum of the fractional uncertainties.

$$\sigma[\mathrm{SWE}] = \left(\frac{\sigma[t]}{t}\right) + \left(\frac{\sigma[v_s]}{v_s}\right) + \left(\frac{\sigma[\rho]}{\rho}\right), \tag{8}$$

where $\sigma[t]$ is 0.4 ns, $\sigma[v_s]$ is 0.01 m/ns, and $\sigma[\rho]$ is 44 kg/m^3. In this study, we estimate that the relative uncertainty in SWE at any point is ±17%.

There are many other sources of uncertainty that contribute to the calculation of B_w, most of which have contributions that are difficult to formally quantify. These include using a single snow density and radar wave velocity at each glacier due to the lack of sufficient observations to justify spatially distributed values. Additionally, the end-of-season scaling (section 3.5) from weather station data may introduce substantial uncertainties, particularly given the strong elevation dependence of SWE and the large lateral distances between the glaciers and their respective stations. However, scaling is required to make interglacier comparisons.

The spatial extrapolation of SWE over the glacier area may be the largest informal uncertainty. Two sources of error arise in the extrapolation: spatial variability of SWE not captured by GPR profiles and weak or potentially erroneous relationships between terrain parameters and SWE. Logistics, objective hazard, and

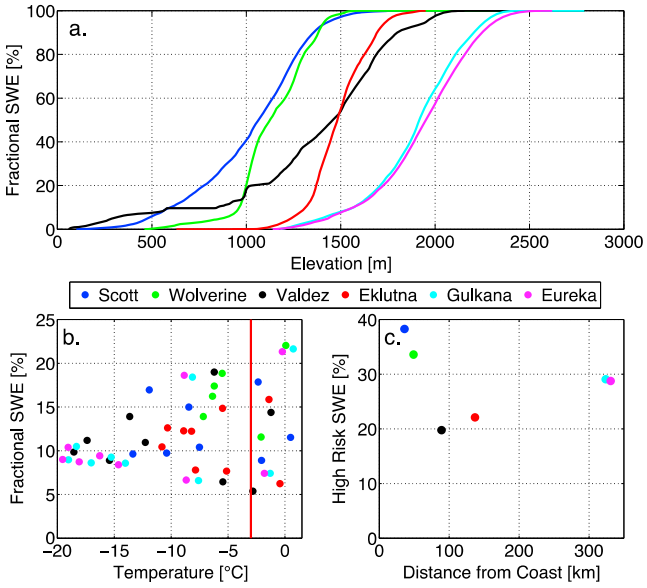

Figure 13. (a) Fractional SWE (normalized by total SWE) as a function of elevation; (b) monthly SWE (as percentage of total winter SWE) plotted as a function of monthly mean temperature, both derived from the PRISM data set; and (c) cumulative high-risk SWE that is susceptible to changing snow/rain fraction. High-risk SWE is identified as falling during months with a mean temperature greater than −3°C.

weather place unavoidable constraints on spatial coverage, but the GPR-forced extrapolation uses several orders of magnitude more observations to estimate B_w than any network of direct observations. Our analyses suggest that presurvey planning to maximize terrain-parameter coverage, rather than solely maximizing spatial extent, will likely lead to more accurate SWE extrapolations.

5.6. Impact of Changing Snow/Rain Fraction

Future climate projections show a substantial increase in rain-on-snow events and an associated decrease in the snow/rain fraction throughout Alaska by the end of the 21st century [*McAfee et al*., 2013]. Our data provide an opportunity to assess the potential impact of this transition on glacier mass balances. For each glacier, we calculated the distribution of total SWE as a function of elevation to link glacier geometries to climate processes and provide a sensitivity parameterization for future climate change. Figure 13a shows that 90% of the total accumulation at Wolverine and Eklutna glaciers is deposited over a narrow ~500 m elevation range, with 50% below 1500 m. In contrast, the 90% range for Valdez Glacier spans ~1600 m, with 50% above ~1500 m. Low-elevation glaciers, and particularly those that collect the majority of their accumulation over narrow elevation ranges, are highly susceptible to increasing temperatures and freezing levels. If the warming occurs during the characteristically wet seasons, the reductions in the snow/rain fraction are likely to be substantial.

A more detailed evaluation of glacier susceptibility to changes in snow/rain fraction can be estimated from the percentage of accumulation deposited when temperatures are near freezing. Each glacier we surveyed is susceptible to substantial changes in the snow/rain fraction for at least 2 months of the accumulation season, when the area-weighted mean temperature is close to 0°C [*McAfee et al*., 2013]. Changes in September and October potentially have the most impact, as historically the largest fraction of high-elevation accumulation occurs during these months (Figure 13b). Our analysis suggests that ~20% of accumulation may change phase to rain even with only 1–2°C warming, which could easily occur by midcentury (Figure 13c) [*Scenarios Network for Alaska and Arctic Planning*, 2015]. This metric suggests that high-elevation, continental glaciers like Gulkana and Eureka appear equally susceptible to shoulder season warming because the peak in precipitation occurs earlier in the year in this region and thus will not be completely insulated from the impacts of climate warming.

6. Conclusions

We quantified SWE at seven glaciers across five Alaskan climate zones at the end of the 2012–2013 winter using ground- and helicopter-based GPR. Geostatistical analyses yielded new insights into SWE distributions over a broad range of spatial scales. Over short decameter scales, we found that SWE variability is larger in characteristically rough ablation zones than it is in accumulation zones where the summer surface is smoother. At the basin or branch scale spatial cross-glacier variability and differences between tributaries can be significant. For some glaciers, estimating this variability is essential to accurately capturing the glacier-wide SWE elevation gradient. SWE elevation gradients reported here (115–400 mm/100 m) exceed those reported for other alpine regions of the world, likely due to the frequent occurrence of split snow-rain

events over the elevation range of an individual glacier. Over regional length scales, SWE decreases with distance from the coast, which serves as an excellent proxy for the principle moisture source.

GPR surveys typically provide several orders of magnitude more observations than typical methodologies and hence, yield a significantly broader view of glacier-wide snow accumulation patterns. However, without ground truth observations, the likelihood of mispicking the annual layer in the accumulation zone can be high. In coastal Alaska, both rain on snow and split rain-snow events frequently form strong internal reflectors that can confound the annual layer identification in the accumulation zone and preclude simply following reflectors upglacier. These difficulties emphasize that GPR is best suited to complement, rather than replace traditional mass balance networks, as these in situ constraints are necessary for both interpretation and density/velocity determination.

By comparing different analysis approaches, we gained insight into the sensitivity of the method for calculating glacier-wide winter balances, B_w. Using multiple linear regressions on limited data sets (i.e., centerline-only profiles) to estimate B_w may not accurately capture glacier-wide distributions due to the limited sampling of the glacier's full distribution of terrain parameters. However, we found close agreement between B_w calculated using multiple linear regressions on the full data sets and a simple hypsometric method using a centerline derived SWE elevation gradients. This agreement is best when B_w estimates were summed across all glaciers, suggesting that centerline surveys of numerous glaciers may be sufficient for capturing regional-scale B_w. However, in this case, B_w estimates should only be calculated using a hypsometric approach, rather than basin-scale terrain-parameter extrapolations.

While uncertainty analysis is challenging, we were able to estimate the accuracy of the technique through comparison with other data sets. At the USGS Benchmark Glaciers, GPR and glaciological B_w estimates vary by 6–36%, with some dependence on the extrapolation method [*O'Neel et al*., 2014]. GPR and PRISM data also broadly agree (9–36% difference).

Linking climate, radar, and basin geometry data shows that each of the surveyed glaciers exhibit substantial susceptibility to predicted warming and associated decreases in the snow/rain fraction. Our results show that glaciers where accumulation is focused over narrow elevation ranges (flat glaciers) are likely to show stronger sensitivity to further warming.

Acknowledgments

Data used in this study are archived at 10.5066/F7M043G7. Funding from the U.S. Geological Survey Climate and Land Use Research and Development program, the U.S. Department of Interior Alaska Climate Science Center, the Oil Spill Recovery Institute, NASA's Cryospheric Sciences Program (NNX11AF41G and NNX15AG21G), and Capital Improvement Project awarded to the Climate and Cryosphere Hazards Program at the Alaska Division of Geological and Geophysical Surveys supported this research. Additionally, we thank Mike Loso for field assistance and funding support (Anchorage Municipal Light and Power and Alaska Pacific University) for Eklutna Glacier; Adam Winstral for sharing the *Sx* code; and Jack Kohler, Clément Miège, and an anonymous reviewer for their constructive comments, which improved the manuscript. Any use of trade, firm, or product names is for descriptive purposes only and does not imply endorsement by the U.S. Government.

References

Anderson, B. T., J. P. McNamara, H. P. Marshall, and A. N. Flores (2014), Insights into the physical processes controlling correlations between snow distribution and terrain properties, *Water Resour. Res.*, *50*, 4545–4563, doi:10.1002/2013WR013714.

Arendt, A., K. Echelmeyer, W. Harrison, C. Lingle, S. Zirnheld, V. Valentine, B. Ritchie, and M. Druckenmiller (2006), Updated estimates of glacier volume changes in the western Chugach Mountains, Alaska, and a comparison of regional extrapolation methods, *J. Geophys. Res.*, *111*, F03019, doi:10.1029/2005JF000436.

Arendt, A., S. Luthcke, A. Gardner, S. O'Neel, D. Hill, G. Moholdt, and W. Abdalati (2013), Analysis of a GRACE global mascon solution for Gulf of Alaska glaciers, *J. Glaciol.*, *59*(217), 913–924, doi:10.3189/2013JoG12J197.

Balk, B., and K. Elder (2000), Combining binary regression tree and geostatistical methods to estimate snow distribution in a mountain watershed, *Water Resour. Res.*, *36*(1), 13–26, doi:10.1029/1999WR900251.

Bieniek, P. A., et al. (2012), Climate divisions for Alaska based on objective methods, *J. Appl. Meteorol. Climatol.*, *51*, 1276–1289.

Booth, A. D., R. A. Clark, and T. Murray (2010), Semblance response to a ground-penetrating radar wavelet and resulting errors in velocity analysis, *Near Surf. Geophys.*, *8*(3), 235–246, doi:10.3997/1873-0604.2010008.

Booth, A. D., R. A. Clark, and T. Murray (2011), Influences on the resolution of GPR velocity analyses and a Monte Carlo simulation for establishing velocity precision, *Near Surf. Geophys.*, *9*(5), 399–411, doi:10.3997/1873-0604.2011019.

Booth, A. D., A. Mercer, R. Clark, T. Murray, P. Jansson, and C. Axtell (2013), A comparison of seismic and radar methods to establish the thickness and density of glacier snow cover, *Ann. Glaciol.*, *54*(64), 73–82, doi:10.3189/2013AoG64A044.

Bradford, J. H., J. T. Harper, and J. Brown (2009), Complex dielectric permittivity measurements from ground-penetrating radar data to estimate snow liquid water content in the pendular regime, *Water Resour. Res.*, *45*, W08403, doi:10.1029/2008WR007341.

Brandt, O., K. Langley, A. Giannopoulos, S.-E. Hamran, and J. Kohler (2009), Radar response of firn exposed to seasonal percolation, validation using cores and FDTD modeling, *IEEE Trans. Geosci. Remote Sens.*, *47*, 2773–2785.

Bühler, Y., M. Marty, L. Egli, J. Veitinger, T. Jonas, P. Thee, and C. Ginzler (2015), Snow depth mapping in high-alpine catchments using digital photogrammetry, *Cryosphere*, *9*(1), 229–243, doi:10.5194/tc-9-229-2015.

Carroll, S. S., and N. Cressie (1996), A comparison of geostatistical methodologies used to estimate snow water equivalent, *J. Am. Water Resour. Assoc.*, *32*, 267–278, doi:10.1111/j.1752-1688.1996.tb03450.x.

Cherry, J. E., S. Walker, N. Fresco, S. Trainor, and A. Tidwell (2010), Impacts of climate change and variability on hydropower in Southeast Alaska: Planning for a robust energy future.

Dai, A. (2008), Temperature and pressure dependence of the rain-snow phase transition over land and ocean, *Geophys. Res. Lett.*, *35*, L12802, doi:10.1029/2008GL033295.

Daly, C., M. Halbleib, J. I. Smith, W. P. Gibson, M. K. Doggett, G. H. Taylor, J. Curtis, and P. P. Pasteris (2008), Physiographically sensitive mapping of climatological temperature and precipitation across the conterminous United States, *Int. J. Climatol.*, *28*, 2031–2064, doi:10.1002/joc.1688.

Dietz, A. J., C. Kuenzer, U. Gessner, and S. Dech (2012), Remote sensing of snow—A review of available methods, *Int. J. Remote Sens.*, *33*(13), 4094–4134, doi:10.1080/01431161.2011.640964.
Dix, C. H. (1955), Seismic velocities from surface measurements, *Geophysics*, *34*, 180–195.
Erxleben, J., K. Elder, and R. Davis (2002), Comparison of spatial interpolation methods for estimating snow distribution in the Colorado Rocky Mountains, *Hydrol. Processes*, *16*(18), 3627–3649, doi:10.1002/hyp.1239.
Gardner, A. S., et al. (2013), A reconciled estimate of glacier contributions to sea level rise: 2003 to 2009, *Science*, *340*, 852–857, doi:10.1126/science.1234532.
Grabiec, M., D. Puczko, T. Budzik, and G. Gajek (2011), Snow distribution patterns on Svalbard glaciers derived from radio-echo soundings, *Pol. Polar Res.*, *32*(4), 393–421, doi:10.2478/v10183-011-0026-4.
Grünewald, T., and M. Lehning (2011), Altitudinal dependency of snow amounts in two alpine catchments: Can catchment-wide snow amounts be estimated via single snow or precipitation stations?, *Ann. Glaciol.*, *52*(58), 153–158.
Grünewald, T., M. Schirmer, R. Mott, and M. Lehning (2010), Spatial and temporal variability of snow depth and ablation rates in a small mountain catchment, *Cryosphere*, *4*(2), 215–225.
Gusmeroli, A., and G. Grosse (2012), Ground penetrating radar detection of subsnow slush on ice covered lakes in interior Alaska, *Cryosphere*, *6*, 1435–1443.
Gusmeroli, A., G. J. Wolken, and A. A. Arendt (2014), Helicopter-borne radar imaging of snow cover on and around glaciers in Alaska, *Ann. Glaciol.*, *55*(67), 78–88, doi:10.3189/2014AoG67A029.
Hill, D. F., N. Bruhis, S. E. Calos, A. Arendt, and J. Beamer (2015), Spatial and temporal variability of freshwater discharge into the Gulf of Alaska, *J. Geophys. Res. Oceans*, *120*, 634–646, doi:10.1002/2014JC010395.
Hock, R. (2005), Glacier melt: A review of processes and their modeling, *Prog. Phys. Geogr.*, *29*, 362–391, doi:10.1191/0309133305pp453ra.
Hood, E., and L. Berner (2009), Effects of changing glacial coverage on the physical and biogeochemical properties of coastal streams in southeastern Alaska, *J. Geophys. Res.*, *114*, G03001, doi:10.1029/2009JG000971.
Hood, E., T. J. Battin, J. Fellman, S. O'Neel, and R. G. M. Spencer (2015), Storage and release of organic carbon from glaciers and ice sheets, *Nat. Geosci.*, *8*, 91–96, doi:10.1038/ngeo2331.
Huffman, G. J., D. T. Bolvin, E. J. Nelkin, D. B. Wolff, R. F. Adler, G. Gu, Y. Hong, K. P. Bowman, and E. F. Stocker (2007), The TRMM Multisatellite Precipitation Analysis (TMPA): Quasi-global, multiyear, combined-sensor precipitation estimates at fine scales, *J. Hydrometeorol.*, *8*, 38–55, doi:10.1175/JHM560.1.
Huss, M., M. Zemp, P. Joerg, and N. Salzmann (2014), High uncertainty in 21st century runoff projections from glacierized basins, *J. Hydrol.*, *510*, 35–48, doi:10.1016/j.jhydrol.2013.12.017.
Immerzeel, W. W., F. Pellicciotti, and M. F. P. Bierkens (2013), Rising river flows throughout the twenty-first century in two Himalayan glacierized watersheds, *Nat. Geosci.*, *6*, 742–745, doi:10.1038/ngeo1896.
Jarosch, A. H., F. S. Anslow, and G. K. Clarke (2012), High-resolution precipitation and temperature downscaling for glacier models, *Clim. Dyn.*, *38*, 391–409, doi:10.1007/s00382-010-0949-1.
Jonas, T., C. Marty, and J. Magnusson (2009), Estimating the snow water equivalent from snow depth measurements in the Swiss Alps, *J. Hydrol.*, *378*, 161–167, doi:10.1016/j.jhydrol.2009.09.021.
Kaser, G., M. Großhauser, and B. Marzeion (2010), Contribution potential of glaciers to water availability in different climate regimes, *Proc. Natl. Acad. Sci. U.S.A.*, *107*, 20,223–20,227, doi:10.1073/pnas.1008162107.
Kaspari, S., P. A. Mayewski, D. A. Dixon, V. B. Spikes, S. B. Sneed, M. J. Handley, and G. S. Hamilton (2004), Climate variability in West Antarctica derived from annual accumulation-rate records from ITASE firn/ice cores, *Ann. Glaciol.*, *39*, 585–594.
Kienholz, C., J. L. Rich, A. A. Arendt, and R. Hock (2014), A new method for deriving glacier centerlines applied to glaciers in Alaska and northwest Canada, *Cryosphere*, *8*, 503–519, doi:10.5194/tc-8-503-2014.
Kohler, J., J. Moore, M. Kennett, R. Engeset, and H. Elevhøy (1997), Using ground-penetrating radar to image previous years' summer surfaces for mass-balance measurements, *Ann. Glaciol.*, *24*, 355–360.
Kovacs, A., A. J. Gow, and R. M. Morey (1995), The in-situ dielectric constant of polar firn revisited, *Cold Reg. Sci. Technol.*, *23*, 245–256.
Lehning, M., T. Grünewald, and M. Schirmer (2011), Mountain snow distribution governed by altitudinal gradient and terrain roughness, *Geophys. Res. Lett.*, *38*, L19504, doi:10.1029/2011GL048927.
L'Heureux, M. L., M. E. Mann, B. I. Cook, B. E. Gleason, and R. S. Vose (2004), Atmospheric circulation influences on seasonal precipitation patterns in Alaska during the latter 20th century, *J. Geophys. Res.*, *109*, D06106, doi:10.1029/2003JD003845.
Machguth, H., O. Eisen, F. Paul, and M. Hoelzle (2006), Strong spatial variability of snow accumulation observed with helicopter-borne GPR on two adjacent Alpine glaciers, *Geophys. Res. Lett.*, *33*, L13503, doi:10.1029/2006GL026576.
Masson-Delmotte, V., et al. (2008), A review of Antarctic surface snow isotopic composition: Observations, atmospheric circulation, and isotopic modeling, *J. Clim.*, *21*, 3359–3387, doi:10.1175/2007JFLI2139.1.
McAfee, S., J. Walsh, and T. S. Rupp (2013), Statistically downscaled projections of snow/rain partitioning for Alaska, *Hydrol. Processes*, *28*(12), 3930–3946, doi:10.1002/hyp.9934.
McCreight, J. L., E. E. Small, and K. M. Larson (2014), Snow depth, density, and SWE estimates derived from GPS reflection data: Validation in the western U.S., *Water Resour. Res.*, *50*, 6892–6909, doi:10.1002/2014WR015561.
Mesquita, M. D. S., D. E. Atkinson, and K. I. Hodges (2010), Characteristics and variability of storm tracks in the North Pacific, Bering Sea, and Alaska, *J. Clim.*, *23*, 294–311, doi:10.1175/2009JCLI3019.1.
Molotch, N. P., and R. C. Bales (2005), Scaling snow observations from the point to the grid element: Implications for observation network design, *Water Resour. Res.*, *41*, W11421, doi:10.1029/2005WR004229.
Molotch, N. P., M. T. Colee, R. C. Bales, and J. Dozier (2005), Estimating the spatial distribution of snow water equivalent in an alpine basin using binary regression tree models: The impact of digital elevation data and independent variable selection, *Hydrol. Processes*, *19*, 1459–1479, doi:10.1002/hyp.5586.
Montgomery, D. C., E. A. Peck, and G. G. Vining (2001), *Introduction to Linear Regression Analysis*, 3rd ed., John Wiley, New York.
Neal, E. G., E. Hood, and K. Smikrud (2010), Contribution of glacier run-off to freshwater discharge into the Gulf of Alaska, *Geophys. Res. Lett.*, *37*, L06404, doi:10.1029/2010GL042385.
Okorn, R., G. Brunnhofer, T. Platzer, A. Heilig, L. Schmid, C. Mitterer, J. Schweizer, and O. Eisen (2014), Upward-looking L-band FMCW radar for snow cover monitoring, *Cold Reg. Sci. Technol.*, *103*, 31–40, doi:10.1016/j.coldregions.2014.03.006.
O'Neel, S., E. Hood, A. Arendt, and L. Sass (2014), Assessing streamflow sensitivity to variations in glacier mass balance, *Clim. Change*, *123*(2), 329–341, doi:10.1007/s10584-013-1042-7.
Pälli, A., J. C. Kohler, E. Isaksson, J. C. Moore, J. F. Pinglot, V. A. Pohjola, and K. Samuelsson (2002), Spatial and temporal variability of snow accumulation using ground-penetrating radar and ice cores on a Svalbard glacier, *J. Glaciol.*, *48*(162), 417–424.

Pelto, M., J. Kavanaugh, and C. McNeil (2013), Juneau icefield mass balance program 1946–2011, *Earth Syst. Sci. Data*, *5*, 319–330, doi:10.5194/essd-5-319-2013.
Pelto, M. S., and M. M. Miller (1990), Mass balance of the Taku Glacier, Alaska from 1946 to 1986, *Northwest Sci.*, *64*(3), 121–130.
Pérez-Ruiz, M., J. Carballido, and J. Agüera (2011), Assessing GNSS correction signals for assisted guidance systems in agricultural vehicles, *Precis. Agric.*, *12*, 639–652, doi:10.1007/s11119-010-9211-4.
Pfeffer, W. T., et al. (2014), The Randolph Glacier Inventory: A globally complete inventory of glaciers, *J. Glaciol.*, *60*(221), 537–552, doi:10.3189/2014JoG13J176.
Previati, M., A. Godio, and S. Ferraris (2011), Validation of spatial variability of snowpack thickness and density obtained with GPR and TDR methods, *J. Appl. Geophys.*, *75*, 284–293.
Revuelto, J., J. I. Lopez-Moreno, C. Azorin-Molina, and S. M. Vicente-Serrano (2014), Topographic control of snowpack distribution in a small catchment in the central Spanish Pyrenees: Intra- and inter-annual persistence, *Cryosphere*, *8*, 1989–2006, doi:10.5194/tc-8-1989-2014.
Roe, G. H. (2005), Orographic precipitation, *Annu. Rev. Earth Planet. Sci.*, *33*, 645–671, doi:10.1146/annurev.earth.33.092203.122541.
Sass, L., S. O'Neel, M. Loso, J. A. MacGregor, G. A. Catania, and C. F. Larsen (2009), Contributions of climate and dynamics to mass wastage and accumulation zone thinning of Eklutna Glacier, Alaska, *Eos Trans. AGU*, *90*(52), Fall Meet. Suppl., Abstract C32A-04.
Scenarios Network for Alaska and Arctic Planning (2015), Regional climate projects, Univ. of Alaska. [Retrieved 1/28/15 from www.snap.uaf.edu/sites/all/modules/snap_map_tool/maps.]
Schirmer, M., V. Wirz, A. Clifton, and M. Lehning (2011), Persistence in intra-annual snow depth distribution: 1. Measurements and topographic control, *Water Resour. Res.*, *47*, W09516, doi:10.1029/2010WR009426.
Sheriff, R. E., and L. P. Geldart (1999), *Exploration Seismology*, 2nd ed., Cambridge Univ. Press, Cambridge, U. K.
Sold, L., M. Huss, M. Hoelzle, H. Andereggen, P. Joerg, and M. Zemp (2013), Methodological approaches to infer end-of-winter snow distribution on alpine glaciers, *J. Glaciol.*, *59*(218), 1047–1059, doi:10.3189/2013JoG13J015.
Stabeno, P. J., N. A. Bond, A. J. Hermann, N. B. Kachel, C. W. Mordy, and J. E. Overland (2004), Meteorology and oceanography of the Northern Gulf of Alaska, *Cont. Shelf Res.*, *24*, 859–897, doi:10.1016/j.csr.2004.02.007.
Taner, M. T., and F. Koehler (1969), Velocity spectra-digital computer derivation and applications of velocity functions, *Geophysics*, *34*(6), 859–881, doi:10.1190/1.1440058.
Van Beusekom, A. E., S. R. O'Neel, R. S. March, L. C. Sass, and L. H. Cox (2010), Re-analysis of Alaskan Benchmark Glacier mass balance data using the index method, *Sci. Invest. Rep. 2010–5247,* 16 pp., U.S. Geol. Surv.
van Pelt, W. J. J., R. Pettersson, V. A. Pohjola, S. Marchenko, B. Claremar, and J. Oerlemans (2014), Inverse estimation of snow accumulation along a radar transect on Nordenskiöldbreen, Svalbard, *J. Geophys. Res. Earth Surf.*, *119*, 816–835, doi:10.1002/2013JF003040.
Weller, J. (2013), Natural Resources Conservation Service Alaska snow survey report, May. [Available at http://www.nrcs.usda.gov/wps/portal/nrcs/main/ak/snow/, accessed 6/1/2014.]
Winstral, A., K. Elder, and R. E. Davis (2002), Spatial snow modeling of wind-redistributed snow using terrain-based parameters, *J. Hydrometeorol.*, *3*, 524–538.
Woo, M.-K., and P. Marsh (1978), Analysis of error in the determination of snow storage for small high Arctic basins, *J. Appl. Meteorol.*, *17*, 1537–1541.
Yelf, R., and D. Yelf (2006), Where is true time zero?, *Electromagn. Phenom.*, *7*(1), 158–163.
Zemp, M., M. Hoelzle, and W. Haeberli (2009), Six decades of glacier mass-balance observations: A review of the worldwide monitoring network, *Ann. Glaciol.*, *50*, 101–111.